ACS APPLIED MATERIALS & INTERFACES

Research Article

www.acsami.org

Magnetic Ionic Liquids Produced by the Dispersion of Magnetic Nanoparticles in 1-*n*-Butyl-3-methylimidazolium bis(trifluoromethanesulfonyl)imide (BMI.NTf$_2$)

Anderson M. M. S. Medeiros,[†] Alexandre L. Parize,[†,‡] Vanda M. Oliveira,[†] Brenno A.D. Neto,[†] Andris F. Bakuzis,[§] Marcelo H. Sousa,[▽] Liane M. Rossi,[⊥] and Joel C. Rubim*[,†]

[†] Laboratório de Materiais e Combustíveis - LMC, Instituto de Química da Universidade de Brasília, CP.04478, 70904-970, Brasília, DF, Brasil.

[‡] Universidade de Brasília, Campus Planaltina, Vila Nossa Sra. de Fátima, 73300-000, Planaltina-DF, Brasil

[§] Faculdade de Ceilândia, Universidade de Brasília, QNN 14 AE, Ceilândia Sul, 72220-140, Ceilândia-DF, Brazil

[▽] Instituto de Física, Universidade Federal de Goiás, 74001-970, Goiânia, GO, Brasil

[⊥] Instituto de Química, Universidade de São Paulo, CP 26077, 05513-970, São Paulo, SP, Brasil

Supporting Information

ABSTRACT: `This paper reports on the advancement of magnetic ionic liquids (MILs) as stable dispersions of surface-modified γ-Fe_2O_3, Fe_3O_4, and $CoFe_2O_4$ magnetic nanoparticles (MNPs) in a hydrophobic ionic liquid, 1-*n*-butyl 3-methylimidazolium bis(trifluoromethanesulfonyl)imide (BMI.NTf$_2$). The MNPs were obtained via coprecipitation and were characterized using powder X-ray diffraction, transmission electron microscopy, Raman spectroscopy and Fourier transform near-infrared (FT-NIR) spectroscopy, and magnetic measurements. The surface-modified MNPs (SM-MNPs) were obtained via the silanization of the MNPs with the aid of 1-butyl-3-[3-(trimethoxysilyl)propyl]imidazolium chloride (BMSPI.Cl). The SM-MNPs were characterized by Raman spectroscopy and Fourier transform infrared−attenuated total reflectance (FTIR-ATR) spectroscopy and by magnetic measurements. The FTIR-ATR spectra of the SM-MNPs exhibited characteristic absorptions of the imidazolium and those of the Fe−O−Si−C moieties, confirming the presence of BMSPI.Cl on the MNP surface. Thermogravimetric analysis (TGA) showed that the SM-MNPs were modified by at least one BMSPI.Cl monolayer. The MILs were characterized using Raman spectroscopy, differential scanning calorimetry (DSC), and magnetic measurements. The Raman and DSC results indicated an interaction between the SM-MNPs and the IL. This interaction promotes the formation of a supramolecular structure close to the MNP surface that mimics the IL structure and is responsible for the stability of the MIL. Magnetic measurements of the MILs indicated no hysteresis. Superparamagnetic behavior and a saturation magnetization of ~22 emu/g could be inferred from the magnetic measurements of a sample containing 50% w/w γ-Fe_2O_3 SM-MNP/BMI.NTf$_2$.

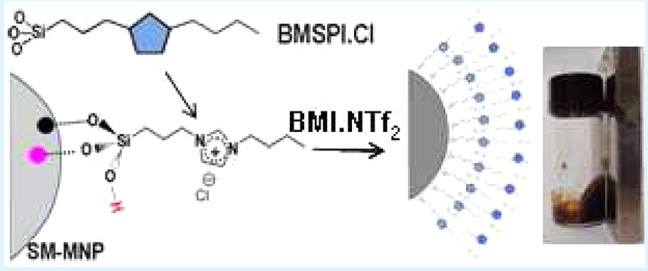

KEYWORDS: *magnetic ionic liquid, ferrofluid, ionic liquid, magnetic nanoparticle, dispersion, stabilization*

INTRODUCTION

Magnetic fluids (MFs) are generally composed of stable dispersions of magnetic nanoparticles (MNPs) in a liquid (or solvent) carrier. The MFs have applications in several areas, such as magnetic transport of drugs[1,2] and hyperthermia.[3,4] Some applications (e.g., magnetic seals) can withstand high-vacuum and ultrahigh-vacuum (10^{-6}−10^{-10} Pa) conditions, that common solvents, such as water and organic solvents, cannot be used. Solvents with low or negligible vapor pressures,[5] e.g., ionic liquids (ILs), must be used in these cases.

Kano et al.[5] obtained an MF with an ultralow vapor pressure (7.0×10^{-10} Pa at 293 K) by modifying the surface of magnetite nanoparticles with surfactants based on acid derivatives of hexafluoropropylene oxide. The nanoparticles were then dispersed in a high-molecular-weight hexafluoropropylene oxide polymer. However, the surfactants and solvents used in this process (organofluorine compounds) have strong environmental impacts, because of their toxicity.

Ionic liquids, particularly those derived from the cation 1,3-dialkylimidazolium, present interesting properties, such as chemical and thermal stability[6] and negligible vapor pressures (e.g., $\sim 10^{-11}$ Pa for 1-*n*-butyl-3-methylimidazolium hexafluorophosphate (BMI.PF$_6$)).[7] These features render the IL a special medium for material production and analysis under high-

Received: July 18, 2012
Accepted: September 11, 2012
Published: September 11, 2012

Scheme 1. Synthesis of the IL BMSPI.Cl (3).[16]

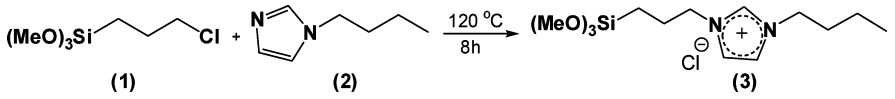

vacuum conditions.[8] Therefore, an alternative solution for the preparation of MFs with negligible vapor pressures requires the use of ILs as solvent carriers. Some research groups have attempted to obtain stable dispersions of magnetic nanoparticles in ILs, or magnetic ionic liquids (MILs). The first attempt to produce an MIL was reported by Hayachi and Hamaguchi;[9] however, their MILs were not made of MNPs but rather by a mixture of $FeCl_3$ and the IL BMI.Cl, leading to the formation of the MIL BMI.$FeCl_4$. This MIL has at least three major drawbacks: (i) lower magnetization, (ii) hydrophilicity, and (iii) low thermal stability. Guerreiro et al.[10] reported the dispersion of magnetite microparticles in ILs (BMI.BF_4 and BMI.PF_6), leading to the formation of a magnetorheological fluid and not an MIL. Recently, we have obtained[11] an MIL consisting of stable dispersions with magnetic maghemite (γ-Fe_2O_3) and $CoFe_2O_4$ nanoparticles in the IL BMI.BF_4. The as-obtained MIL was unstable in the presence of water (BMI.BF_4 is highly hydrophilic), and stable dispersions of these MNPs could not be achieved with either BMI.PF_6 or BMI.NTf_2. Jain et al. obtained MILs based on the dispersion of polymer-coated maghemite MNPs in both protic ethylammonium and aprotic imidazolium in room-temperature ILs.[12] Stable dispersions of Fe_3O_4 MNPs in the IL, 1-ethyl-3-methylimidazolium ethylsulfate, were obtained by Rodriguez-Arco et al.,[13,14] who modified the surface of the MNP with oleic acid. An excess of oleic acid was then added to the IL to promote the stabilization of the colloidal solution.

Apart from a low vapor pressure, a magnetic fluid for vacuum and high-vacuum applications requires hydrophobicity with high chemical and thermal stability. The IL BMI.NTf_2 fills these requirements, and, to our knowledge, no previous reports can be found in the literature indicating the formation of stable dispersions of MNPs in BMI.NTf_2. Our research shows that stable MILs based on the dispersion of MNPs in BMI.NTf_2 can be obtained. This material is a candidate for use as a magnetic seal in high-vacuum applications.

To achieve our goal, MNPs were synthesized from magnetite (Fe_3O_4), maghemite (γ-Fe_2O_3), and cobalt ferrite ($CoFe_2O_4$) with their surfaces chemically modified to disperse in the IL. We describe the synthesis of the MNPs, their surface modifications, and their dispersion in the IL, leading to the formation of stable MILs. The MNPs and the surface-modified MNPs were characterized using conventional techniques, and the MILs were characterized using Raman spectroscopy, which can provide spectral information on the IL and the MNPs. Finally, a preliminary model will be proposed for the interaction of the surface-modified MNPs and the IL.

EXPERIMENTAL SECTION

Reagents. The analytical-grade reagents $FeCl_3{\cdot}6H_2O$ (97%), $CoCl_2{\cdot}6H_2O$ (98%), $FeSO_4{\cdot}7H_2O$ (99%) (ACROS), NaOH, 1-butanol, triethylamine, methanesulfonyl chloride (VETEC), $LiNTf_2$, $(CH_3)_4NOH$, (3-chloropropyl)trimethoxysilane, and 1-butylimidazole (Sigma–Aldrich) were used as-received. 1-Methylimidazole was distilled prior to use.

Synthesis of the ILs. The IL 1-*n*-butyl-3-methylimidazolium bis(trifluoromethanesulfonyl)imide (BMI.NTf_2) used in the MIL synthesis was prepared using a halide-free method[15] with some modifications.[11]

Synthesis of 1-*n*-Butyl-3-(3-trimethoxysilylpropyl)-imidazolium Chloride (BMSPI.Cl). The surface modifier was prepared according to the procedure by Abu-Reziq et al.,[16] in which (3-chloropropyl)-trimethoxysilane (**1**) reacts with *n*-butylimidazole (**2**) to produce the IL 1-*n*-butyl-3-(3-trimethoxysilylpropyl)imidazolium chloride (BMSPI.Cl, **3**) (see Scheme 1).

Synthesis of the MNPs and the Surface-Modified MNPs (SM-MNPs). Fe_3O_4 and $CoFe_2O_4$ MNPs were obtained via the coprecipitation method.[17,18] The γ-Fe_2O_3 MNPs were obtained by hydrothermally treating Fe_3O_4 MNPs with HNO_3 and $Fe(NO_3)_3$. In this process, the Fe_3O_4 MNPs were oxidized to γ-Fe_2O_3.[19]

The SM-MNPs were obtained by dispersing 6.0–6.5 g of the as-prepared MNPs in 500 mL of ethanol (EtOH, 95%), followed by sonication for 60 min. To this colloidal solution, a 100-mL solution containing 6 mmol (1.94 g) of BMSPI.Cl (**3**) in EtOH and 2 mL of concentrated ammonia (29% aqueous solution) was added under vigorous mechanical stirring. This mixture was allowed to react under a N_2 atmosphere with mechanical stirring for 36 h. The synthesis of the SM-MNPs is represented in Scheme 2.

Scheme 2. Reaction of MNP with the BMSPI.Cl 3 To Form the SM-MNP

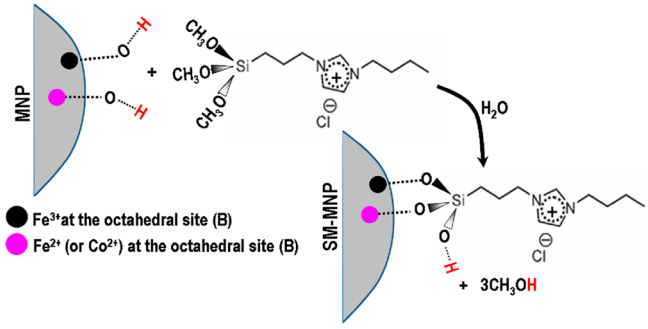

The γ-Fe_2O_3, Fe_3O_4, and $CoFe_2O_4$ MNPs contain M–OH groups (M = Fe^{2+}, Fe^{3+} or Co^{2+}) on their surfaces.[17,20−22] Therefore, according to Scheme 2, a direct substitution reaction occurs, leading to the formation of a modified structure that incorporates the imidazolium moiety.

Synthesis of the MILs. The SM-MNPs were separated from the reaction flask with the aid of a Nd magnet and washed at least three times with 100 mL of EtOH. The SM-MNPs were then dispersed into 400 mL of methanol and stirred mechanically for 30 min. Acetone was added to precipitate the SM-MNPs, which were then separated by use of the Nd magnet. The resulting solid was washed several times with acetone and heated in an oven at 120 °C for 90 min. Finally, the SM-MNPs were added to the IL (30% w/w to 50% w/w) and sonicated for 30 min. The resulting material was a liquid that responds to the presence of magnetic fields (seeFigure 1S in the Supporting Information (SI)).

Instrumentation. X-ray diffraction (XRD) patterns were obtained using a Bruker AXS D8 FOCUS XRD instrument with the generator operating at 40 mA and 30 kV, with Cu Kα radiation (λ = 1.5406 Å) selected by a graphite monochromator.

Transmission electron microscopy (TEM) was performed on a Philips CM200 electron microscope operating at an accelerating voltage of 200 kV. The samples were prepared by collecting a drop of sample suspended in a suitable solvent on carbon-coated copper grids covered by Formvar thin films (Ted Pella, Inc.), followed by air drying.

dx.doi.org/10.1021/am301367d | ACS Appl. Mater. Interfaces 2012, 4, 5458–5465

The average sizes of the MNPs were estimated by measuring two dimensions of 300 nanoparticles. Counting was accomplished with the aid of Image Tools 3.0 software, and the corresponding histograms for the particle size distribution were built using Origin 8.0 software.

The Raman spectra were acquired on a Renishaw inVia Raman system equipped with a Leica microscope and were excited by the 785-nm laser line from an AlGaAs diode laser (Renishaw). The spectra were collected in the backscattering configuration using a 50× objective. The laser power on the sample was adjusted to avoid sample decomposition.

The Fourier transform near-infrared (FT-NIR) spectra of the MNPs dispersed in KBr pellets were recorded on an Equinox 55 spectrometer (Bruker) equipped with a germanium detector. The spectra were acquired using a transflectance accessory, and each spectrum represents the sum of 32 scans at a resolution of 16 cm^{-1}.

The FTIR spectra of the samples dispersed in KBr pellets were obtained on a Shimadzu IR-Prestige 21 system using an attenuated total reflectance (ATR) cell (MIRacle from PIKE Technologies) with a ZnSe prism. Each FTIR spectrum is the result of 32 scans at a resolution of 4 cm^{-1}.

Thermogravimetric analysis (TGA) was performed on a Shimadzu TG-60 system. During scanning, the system was purged with N_2 at a rate of 50 mL min^{-1}. The average sample weight was 10 mg, and a temperature ramp from 25 °C to 800 °C was applied at a heating rate of 10 °C min^{-1}.

The phase transitions of BMI.NTf_2 and the MILs were determined using a differential scanning calorimetry (DSC) (Shimadzu, Model DSC-60) device that was equipped with a manual cooling unit. Prior to the DSC analysis, the instrument was calibrated using zinc. An average sample weight of 10−20 mg was sealed in an aluminum pan. The samples were cooled to −120 °C and subsequently heated to 80 °C at a rate of 5 °C min^{-1} under a N_2 flow.

The magnetic measurements were carried out using a vibrating sample magnetometer (VSM) from ADE Magnetics (Model EV7), operating at a vibrational frequency of 75 Hz. The hysteresis loops (M vs H) of the samples were acquired under applied magnetic fields varying from −20 kOe to +20 kOe at 300 K.

The viscosity measurements were performed at shear rates varying from 0.1 s^{-1} to 1000 s^{-1} on a Physica MCR 301 rheometer (Anton Paar GMB). All of the measurements were performed using a Peltier element for temperature control. Prior to testing, each sample was maintained for 10 min at the test temperature to ensure thermal homogeneity. The equipment was located in a climate-controlled room (20 °C) on an antivibration table (TMC-SYS 63-561).

RESULTS AND DISCUSSION

Characterization of the MNPs. The crystalline structures of the MNPs and their mean sizes were evaluated using powder XRD (see Figure 1). All three types of MNPs presented Bragg reflections, corresponding to the (220), (311), (400), (422), (511), and (440) indexed planes. These reflections are characteristic of spinel ferrites with cubic symmetry.[11] The XRD data could not distinguish among the three types of MNPs. The mean diameters of the MNPs were calculated using the Scherrer equation with the full width at half-maximum (fwhm) of the most intense peak (311).[11] The mean diameters are presented in Table 1.

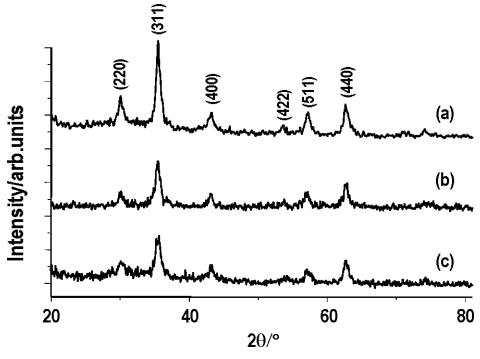

Figure 1. XRD patterns of MNPs: (a) Fe_3O_4, (b) $CoFe_2O_4$, and (c) γ-Fe_2O_3.

Table 1. Mean Diameter of MNPs as Obtained by XRD and TEM

MNP	mean diameter (nm)	
	XRD	TEM
Fe_3O_4	12.3	12.6 ± 1.9
$CoFe_2O_4$	11.0	10.5 ± 1.8
γ-Fe_2O_3	9.9	12.5 ± 2.1

The TEM micrographs of the MNPs show nearly spherical nanoparticles (see Figures 2a, 2c, and 2e), and the corresponding histograms (Figures 2b, 2d, and 2f) indicate that the average sizes agree with the XRD results (see Table 1).

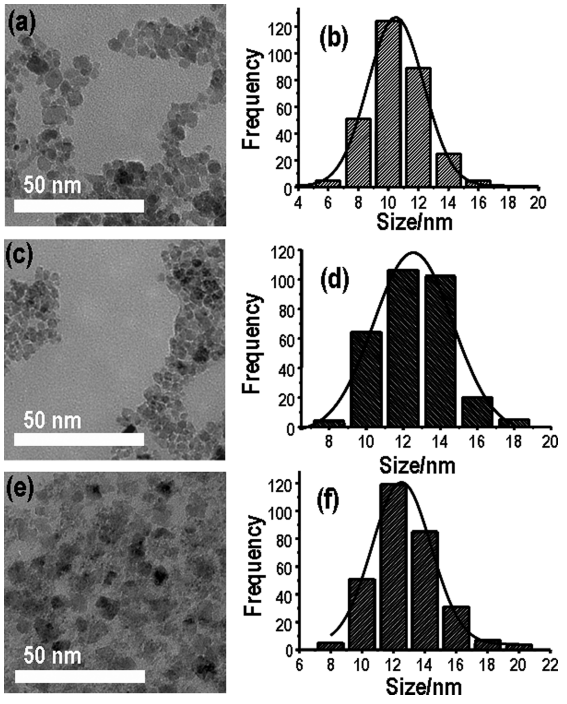

Figure 2. (a, c, e) TEM micrographs of MNPs and (b, d, f) their corresponding histograms: (a, b) γ-Fe_2O_3, (c, d) Fe_3O_4, and (e, f) $CoFe_2O_4$.

Raman spectroscopy is a powerful tool in the characterization of ferrites.[17,20,23] To distinguish among the different magnetic materials, the Raman spectra of solid (powder) samples were recorded (Figure 3). The Raman spectrum of the γ-Fe_2O_3 MNPs (Figure 3a) presented Raman signals at 173, 340, 490, 664, and 705 cm^{-1}, which are characteristic of this type of ferrite.[21] The signal at 705 cm^{-1} represents the oxidation of Fe(II) to Fe(III) at the octahedral sites.[21] The Raman spectrum of the Fe_3O_4 MNPs (Figure 3b) contains at least two characteristic signals of this type of material at 302 and 662 cm^{-1}, which are assigned to the phonons of e_g and a_{1g} symmetry, respectively.[17,24] However, other Raman features appear in the spectrum found in Figure 3b that coincide with

dx.doi.org/10.1021/am301367d | ACS Appl. Mater. Interfaces 2012, 4, 5458−5465

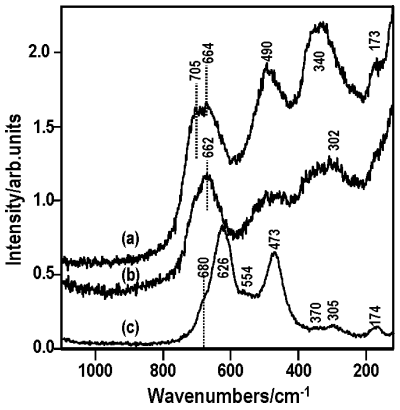

Figure 3. Raman spectra of the MNP: (a) γ-Fe_2O_3, (b) Fe_3O_4, and (c) $CoFe_2O_4$.

the Raman signals of the γ-Fe_2O_3, suggesting partial oxidation of the magnetite to maghemite, given that the spectrum was recorded in air. The $CoFe_2O_4$ MNPs (Figure 3c) presented Raman features at 174, 305, 473, 554, 626, and 680 cm^{-1}. The wavenumber positions and relative intensities of these signals are similar to those reported for $CoFe_2O_4$ nanoparticles.[17]

It is known that Fe_3O_4 and $CoFe_2O_4$ ferrites have characteristic absorption bands in the near-infrared (NIR) region,[17,21] while γ-Fe_2O_3 does not absorb in this spectral region.[25] To further characterize the MNPs, the FT-NIR spectra of the Fe_3O_4 and $CoFe_2O_4$ MNPs were recorded (see Figure 2S in the SI). The Fe_3O_4 MNPs exhibited a broad absorption centered at ~1428 nm (see Figure 2Sa in the SI), which is characteristic of magnetite.[25]

The FT-NIR spectrum of the $CoFe_2O_4$ MNPs (Figure 2Sb in the SI) exhibited two absorption bands: one at 1330 nm with a shoulder at ~1440 nm, and another at 1640 nm. The band at 1440 nm is likely due to an electronic transition of the Fe^{2+} in ferrite,[26] while the band at 1330 nm can be attributed to the transition $^4\Gamma_4(F) \rightarrow {}^4\Gamma_5(F)$ of the Co^{2+} in the octahedral sites. The absorption at ~1640 nm is due to the electronic transition $^4\Gamma_2(F) \rightarrow {}^4\Gamma_4(F)$ of the Co^{2+} ions in the tetrahedral sites.[27] The FT-NIR spectrum of the γ-Fe_2O_3 MNPs is not shown because, as expected, there was no absorption in this spectral region.[25]

The magnetic behavior of the MNPs was evaluated by the magnetic field dependence of the magnetization $M(H)$, represented by the hysteresis loops provided in Figure 4. The

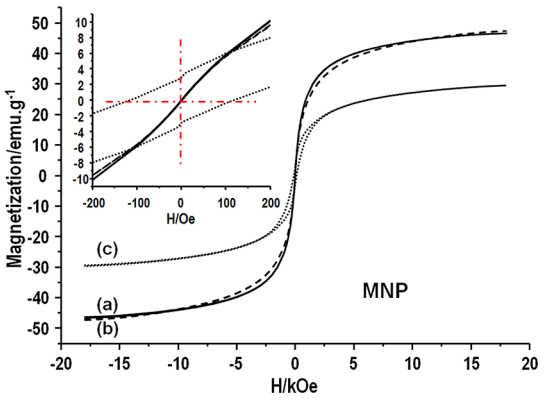

Figure 4. Hysteresis loops at 300 K for the MNPs: (a) γ-Fe_2O_3, (b) Fe_3O_4, (c) $CoFe_2O_4$. The inset shows an enlarged view of the loops in the −200 Oe to +200 Oe region.

results of the saturation magnetization (M_s), remanent magnetization (M_r), and coercive field (H_c) for each type of MNP are displayed in Table 2. Note that the curves for the γ-Fe_2O_3 and Fe_3O_4 MNPs present no hysteresis with negligible values of remanence and coercivity, indicating that these MNPs exhibit superparamagnetic behavior.[28] However, the $CoFe_2O_4$ MNPs present relatively high values of remanence and coercivity, as expected for this type of material when prepared via the coprecipitation method.[22] This high remanence and coercivity clearly indicates that several cobalt-ferrite nanoparticles are in the blocked state, as expected, because of the higher magnetic anisotropy value.

Characterization of SM-MNPs. The TEM analysis shows that the mean diameters and size distribution of the investigated SM-MNPs do not present significant changes in comparison with the MNPs (see Figure 3S in the SI). The observed increase in the mean diameters is within the experimental error. To characterize the SM-MNPs, Raman spectra of the materials were also recorded (see Figure 4S in the SI). However, the Raman spectra of the SM-MNPs samples indicated the same features observed in the Raman spectra of the MNPs. The Raman spectrum of the Fe_3O_4 SM-MNPs sample exhibited a smaller contribution from the maghemite signals, compared with that of the Fe_3O_4 MNPs sample. The presence of the modifier (BMSPI.Cl) on the MNP surface is believed to inhibit the oxidation of magnetite to maghemite. However, in this case, the Raman spectra provided no information about the presence of BMSPI.Cl on the MNP surface.

The FT-NIR spectra of the SM-MNPs and the FT-NIR spectrum of BMSPI.Cl were also recorded (see Figure 5S in the SI). The FT-NIR spectra of the SM-MNPs did not present any absorption that could be assigned to BMSPI.Cl. The only observed absorption bands were those reported in Figure 2S in the SI.

To characterize the presence of BMSPI.Cl on the SM-MNP surface, the FTIR-ATR spectra were obtained for the investigated samples (see Figure 5) (for comparison purposes, see the FTIR spectra of the MNPs shown in Figure 6S in the SI). The tentative assignments for the IR absorptions indicated in Figure 5 are presented in Table 3. Because BMSPI.Cl has an imidazolium moiety, the observation of absorption bands related to imidazolium vibrations clearly indicates that the modifier is present on the MNP surface. The absorption bands at 3134 and 3074 cm^{-1} (imidazolium CH stretching modes),[2,29,30] presented in the inset of Figure 5 demonstrate modification of the MNP surface. The absorption at 2960 cm^{-1} is usually assigned to CH_2 stretching of the butyl group.[2,29,30] The absorption observed at 1563 cm^{-1} is also characteristic of the imidazolium ring and is assigned to imidazolium ring stretching.[30]

Some of the BMSPI.Cl may not have reacted with the surface due to hydrolysis, resulting in the formation of silanol groups (SiOH) (see Scheme 2). The presence of silanol groups is indicated by the absorption bands at 3670 cm^{-1} and 881 cm^{-1}, which are assigned to the SiO−H and Si−OH stretching modes[31] of the hydrolyzed BMSPI.Cl, respectively. In pure BMSPI.Cl, the IR absorptions at 1084 and 1190 cm^{-1} correspond to the Si−O and Si−C stretching vibrations of the methoxysilane groups (C−Si−OCH_3), respectively.[31] As depicted in Scheme 2, during the surface reaction, methanol molecules are released, and the C−Si−OCH_3 moiety is replaced by a C−Si−O−Fe moiety. As a result, the absorption

dx.doi.org/10.1021/am301367d | ACS Appl. Mater. Interfaces 2012, 4, 5458−5465

Table 2. Magnetization Saturation (M_s), Remanence (M_r) and Coercivity (H_c) Values, as Obtained for MNPs, SM-MNPs, and MIL

	MNPs			SM-MNPs			MIL		
	γ-Fe_2O_3	Fe_3O_4	$CoFe_2O_4$	γ-Fe_2O_3	Fe_3O_4	$CoFe_2O_4$	γ-Fe_2O_3	Fe_3O_4	$CoFe_2O_4$
M_s (emu g^{-1})	46.7	47.3	29.6	49.0[a]	48.2[a]	27.0[a]	45.7[a]	30.4[a]	26.7[a]
M_r (emu g^{-1})	0.04	0.05	2.9	0.1[a]	0.04[a]	2.3[a]	0.02[a]	0.02[a]	2.54[a]
H_c (Oe)	0.6	0.6	116	1.8	0.7	87	0.04	0.03	55

[a]The M_s and M_r values were divided by the mass of magnetic material: $m(\gamma\text{-}Fe_2O_3)$ = 0.5013 g; $m(Fe_3O_4)$ = 0.2123 g; $m(CoFe_2O_4)$ = 0.3733 g.

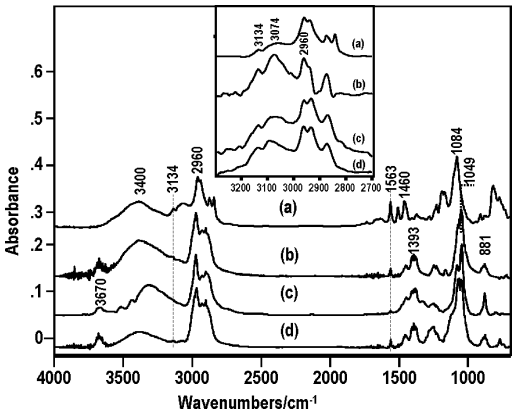

Figure 5. FTIR-ATR spectra of (a) SM = BMSPI.Cl, (b) SM-Fe_3O_4, (c) SM-γ-Fe_2O_3, and (d) SM-$CoFe_2O_4$. The inset shows the DRIFT spectra of the corresponding SM-MNPs at the CH stretching region.

Table 3. Tentative Vibrational Assignment for the IR Absorptions Observed in the Spectra of Figure 5

wavenumber (cm^{-1})	tentative assignment
881	ν(Si−OH)
1049	ν_{as}(Fe−O−Si−O−C)
1084	ν_{as}(Si−O−C)
1190	see text
1393	see text
1460	$\beta(CH_2)$
1563	ν_{str} imidazolium ring
2960	ν_{str} (CH_2)-butyl
3074	ν(CH) imidazolium ring
3136	ν(CH) imidazolium ring
3377 (broad)	ν(H−O−H)
3670	ν(SiO−H)

at 1190 cm^{-1} is not observed for the SM-MNPs, while a new absorption appears at 1049 cm^{-1}, which is tentatively assigned to the Si−C stretching vibration of the C−Si−O−Fe moiety.

The absorption observed at ∼1460 cm^{-1} is characteristic of the CH_2 bending mode.[17] Note that a broad band centered at 1393 cm^{-1} appears after the surface reaction. This feature is not observed in the spectrum of free BMSPI.Cl (see Figure 5a). However, the CH_2 and CH_3 groups present C−H bending modes that usually appear in this spectral region.[17]

To estimate the quantity (surface monolayers) of BMSPI.Cl present on the surface of the SM-MNPs, thermogravimetric analysis (TGA) of the samples (MNPs and SM-MNPs) was performed (see Figure 7S in the SI).

Based on the mass of the BMSPI.Cl present on the SM-MNPs (see Table 4), their surface coverage (θ) can be estimated in terms of BMSPI.Cl monolayers. Table 4 provides the estimated θ values and the parameters used in this evaluation.

Table 4. Surface Coverage (θ), as Estimated from MNPs Density (ρ), Mean XRD Diameter (d), Mass (m_{MNPs}), and Mass of Surface Modifier (m_{sm}, BMSPI.Cl) as Obtained from TGA

SM-MNPs	ρ (g cm^{-3})	d (nm)	m_{MNPs} (mg)	m_{sm} (mg)	θ
Fe_3O_4	5.15	12.3	8.7	0.4	0.9
γ-Fe_2O_3	4.6	9.9	6.7	0.7	1.3
$CoFe_2O_4$	5.3	11.0	4.3	0.4	1.7

Assuming that the MNPs are spherical, the volume of a particular MNP can be calculated by taking into account its mean diameter, as obtained by XRD. Using the density of the MNP as reported in the literature, the mass of one MNP was evaluated. Then, from the mass of the MNP obtained using TGA (m_{MNPs}), the total number of MNPs in the sample and the corresponding surface area (A_{MNP}) were estimated. The number of BMSPI.Cl units present in the mass of the surface modifier (m_{sm}) was calculated, taking into account the molar mass of BMSPI.Cl (322.15 g mol^{-1}). The total area occupied by the BMSPI.Cl units (A_{sm}) was calculated, assuming that a BMSPI.Cl unit occupies 1 nm^2. This assumption is based on the fact that the cross section of the unit cell of the BMI.Cl IL crystal is almost 1.2 nm^2.[32] The θ values displayed in Table 4 were estimated using the A_{sm}/A_{MNP} area ratio. These results indicated that the MNPs are covered by at least one monolayer of BMSPI.Cl, as suggested by the FTIR measurements.

To evaluate the effect of BMSPI.Cl coverage on the magnetization of the SM-MNPs, hysteresis loops were recorded at 300 K (see Figure 8S in the SI,). The saturation magnetization (M_s), remanent magnetization (M_r), and coercive field (H_c) for the SM-MNPs are displayed in Table 2. As observed for the MNPs, the $CoFe_2O_4$ SM-MNPs present non-negligible values for the remanence and coercivity, while the other two SM-MNPs display superparamagnetic behavior. The values of the saturation magnetization (M_s) of the SM-MNPs (normalized to the mass of the magnetic material) are similar to the M_s values obtained for the original MNPs, indicating that the MNP magnetization behavior is preserved after the silanization process. In addition, for the cobalt-ferrite nanoparticle, a 33% decrease was observed in the coercive field after the adsorption of the coating layer. If the size distribution had not changed significantly after the SM-MNP magnetic separation procedure, this result would suggest a strong interaction between the coating layer and the surface atoms. Such behavior might be related to a decrease in the effective magnetic anisotropy, or after the silanization process, it might be due to a surface anisotropy contribution.

Characterization of the MILs. The MILs investigated using Raman spectroscopy correspond to dispersions of SM-MNPs in BMI.NTf_2 in a 25% w/w ratio (SM-MNP:IL). The use of higher SM-MNP concentrations was not possible

because the MILs are dark in color and the scattered radiation is absorbed by the MILs, leading to a poor signal-to-noise ratio.

The Raman spectrum of the γ-Fe_2O_3 MIL (25% w/w) is presented in Figure 6b. For comparison purposes, the Raman

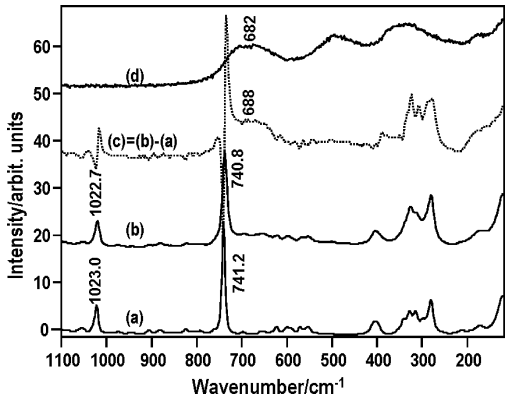

Figure 6. Raman spectra of (a) BMI.NTf_2, (b) γ-Fe_2O_3 MIL, (c) the difference spectra (spectrum b − spectrum a), and (d) SM-γ-Fe_2O_3.

spectrum of the BMI.NTf_2 IL is presented in Figure 6a. Note that the Raman signals of the SM-MNPs dispersed in the IL are difficult to observe in Figure 6b, because the IL exhibits higher light scattering than the MNPs. To recover the Raman spectra of the SM-MNPs, the IL spectrum (Figure 6a) was digitally subtracted from the MIL spectrum (Figure 6b), resulting in the spectrum shown in Figure 6c. In this spectrum, the broad Raman signal of γ-Fe_2O_3 is centered at 688 cm^{-1}, while in the spectrum of the SM-MNPs, it is centered at 682 cm^{-1} (Figure 6d). The Raman signal characteristic of the NTf_2^- anion in the MIL (Figure 6b) is slightly shifted to lower wavenumbers than in the Raman spectrum of the pure IL (Figure 6a). The Raman signal characteristic of the imidazolium ring at 1023 cm^{-1} is also shifted to lower wavenumbers in the MIL. These shifts in the Raman signals for the IL cause a derivative-like peak in the difference spectrum (Figure 6c). Similar results were observed for the other MILs (see Figure 9S in the SI): the Raman signals characteristic of the SM-MNPs dispersed in the IL are shifted to higher wavenumbers than those of the SM-MNPs. The observed shifts for the IL and SM-MNPs Raman signals suggest an interaction between the SM-MNPs and the IL.

The presence of interactions between the SM-MNPs and the IL might cause changes in the DSC of the MILs, in comparison with that of the pure IL. Thus, the DSC curves of the pure IL and those of the 25% w/w MIL were recorded (see Figure 10S in the SI). The relevant data extracted from the DSC curves included the temperatures corresponding to the glass transitions and the melting points, which are displayed in Table 5. All of the MILs presented glass transition and melting

Table 5. Glass Transition (T_g) and Melting Point (T_m) Temperatures as Obtained from the DSC Analysis

sample	T_g (°C)	T_m (°C)
BMI.NTf_2[a]	(−104) to (−86)	−4.0
BMI.NTf_2	−86	−4.9
Fe_3O_4-MIL	−91	−3.4
γ-Fe_2O_3-MIL	−89	−3.4
$CoFe_2O_4$-MIL	−87	−4.1

[a]From refs 33, 34, 35, and 36.

point temperatures shifted slightly from those of the pure IL, suggesting that a weak interaction exists between the SM-MNPs and the IL, which is corroborated by the Raman results.

To evaluate the magnetic behavior of the MIL and its stability, hysteresis loops were recorded as $M(H)$ curves for the investigated MILs (see Figure 11S in the SI). The curves for the γ-Fe_2O_3 MIL correspond to a dispersion of 50% (w/w) γ-Fe_2O_3−SM-MNPs in BMI.NTf_2, while for the other MILs, the relative mass of SM-MNPs was 30% (w/w). This difference occurred because the 50% (w/w) MILs derived from Fe_3O_4 and $CoFe_2O_4$ SM-MNPs were not stable: aggregation could be noted after some hours.

The magnetization curves presented in Figure 11S in the SI are related to the ratio of the magnetic moment to the amount of magnetic mass, which was obtained via TGA (see Table 4 and Figure 7S in the SI). The magnetic parameters of these samples are displayed in Table 2. As observed for the MNPs and SM-MNPs, the $CoFe_2O_4$ nanoparticles dispersed in the IL are in the blocked state, while the other two MILs display superparamagnetic behavior. The coercive fields of the MILs decreased with respect to the MNPs and SM-MNPs, although the remanence was preserved. This apparent decrease should be analyzed carefully, because it could be attributed to the Brownian relaxation mechanism expected only when the nanoparticles are in the liquid carrier. The value of the saturation magnetization (M_s) normalized to the mass of the magnetic material changed for the Fe_3O_4-MIL and was preserved for the other two MILs. This change strongly suggests an oxidation process, most likely due to the heat-treatment procedure. Magnetite is more susceptible to transformation into maghemite (or other iron oxide structures). A careful investigation of the Raman spectra provides strong support for such supposition and explains the observed decrease in the saturation magnetization (see Figures 9SA and 12S in the SI).

Based on the previously reported results, a proposed schematic for the stabilization mechanism of the SM-MNPs surrounded by the IL is presented in Figure 7. The structure of the first layer corresponds to the silanization of the MNP surface by BMSPI.Cl. The strong interactions through the Si−O−Fe bonds are responsible for maintaining the MNPs with the remaining butylimidazolium groups on their surfaces. The surface structures of the SM-MNPs approach that of the BMI.NTf_2 IL, except that Cl serves as the counterion. Once the SM-MNPs are placed in contact with the BMI.NTf_2 IL, the Cl^- ions are replaced by the NTf_2^- ions, which are present in excess. The first surface layer obtains a structure similar to that of the BMI.NTf_2 IL, allowing the formation of supramolecular anionic aggregates analogous to those proposed for the stabilization of metallic[37] and magnetic NPs[11] in ILs. This supramolecular structure acts as a physical barrier to prevent particle aggregation and therefore promotes the stabilization of the MIL.

Per the suggestion of a reviewer, we performed viscosity measurements. Unfortunately, because of experimental limitations, we were not able to obtain viscosities in the presence of a magnetic field. The dynamic viscosity for the BMI.NTf_2 IL was 58 cP, while those for the γ-Fe_2O_3 MILs with 30 and 50% (w/w) MIL, were 336 and 493 cP, respectively. The maghemite MILs were chosen for the viscosity measurements, because of their higher stability, compared with the other samples. Despite the relative increase in the viscosity as the SM-MNPs were added to the IL, all three fluids, including the 50% MIL,

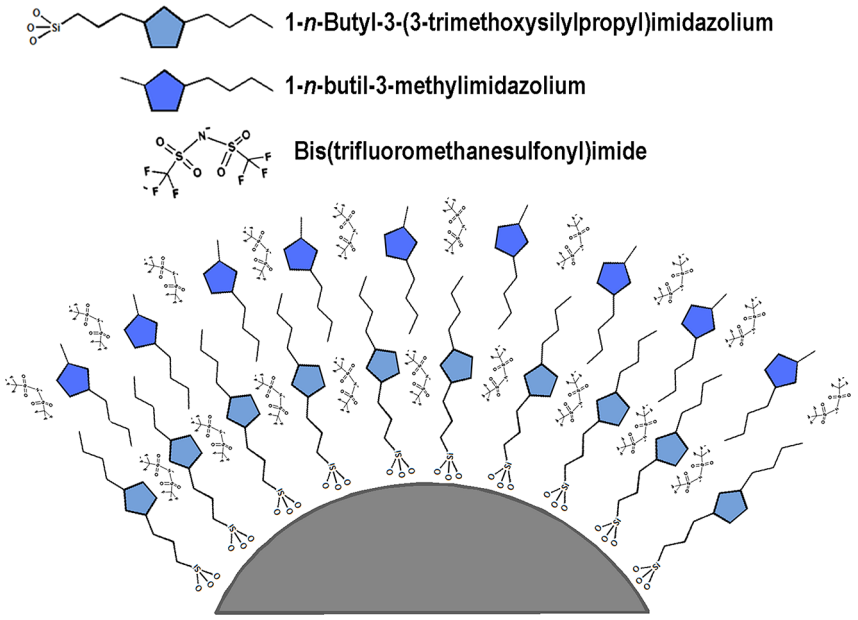

Figure 7. Schematic representation of the SM-MNP and the protective layer formed by supramolecular aggregates in BMI.NTf$_2$.

presented Newtonian behavior. This behavior was confirmed by the dynamic viscosities that remain constant with increasing shear rate (see Figure 13S in the SI), indicating an absence of particle aggregation.

CONCLUDING REMARKS

We have shown that MNPs of γ-Fe_2O_3, Fe_3O_4, and $CoFe_2O_4$ synthesized via coprecipitation present average sizes of 9.3, 12.3, and 11.0 nm, respectively. These MNPs can be easily modified using a silanization process to form surface-modified MNPs (SM-MNPs) with magnetizations close to the parent MNPs. As confirmed by FTIR spectroscopy, the SM-MNPs contain positively charged imidazolium moieties on their surfaces. The SM-MNPs are covered by at least one monolayer of a surface modifier (BMSPI.Cl), as demonstrated via FTIR and TGA analysis. After surface modification, stable dispersions of the γ-Fe_2O_3 SM-MNPs in the IL were obtained in concentrations as high as 50% w/w. The Raman spectra and the DSC results indicated that an interaction exists between the SM-MNPs and the IL BMI.NTf$_2$. This interaction is responsible for the shifts observed in the IL Raman signals and for the Raman phonons of the MNPs, as well as shifts in the glass-transition and melting-point temperatures, compared with those the pure IL. The 30%−50% (w/w) MILs were also shown to be stable in the presence of high magnetic fields without phase separation. Furthermore, the saturation magnetization values of the cobalt-ferrite and maghemite-based nanoparticles were not affected by the silanization process. The same was not observed for the magnetite nanoparticles, most likely because of an enhanced oxidation process after the heat-treatment procedure. The stability of these MILs were attributed to the formation of a supramolecular structure surrounding the MNPs that mimics the structure of the IL and acts as a barrier preventing particle aggregation, which was also confirmed by the Newtonian fluid behavior of the maghemite MIL.

ASSOCIATED CONTENT

Supporting Information

Pictures of the MIL in the absence and presence of a magnetic field (Figure 1S); TEM analysis of the SM-MNP (Figure 2S); FTNIR spectra of MNP (Figure 3S); Raman spectra of SM-MNP (Figure 4S); FTNIR spectra of SM-MNP (Figure 5S); FTIR spectra of the MNP, before surface modification (Figure 6S); TGA of MNP and SM-MNP (Figure 7S); hysteresis loops for the SM-MNP (Figure 8S); Raman spectra of MIL (Figure 9S(A and B)); DSC curves for the MIL (Figure 10S); hysteresis loops for the MIL (Figure 11S); Raman spectra of heated SM-Fe_3O_4 sample (Figure 12S); viscosity−shear rate curves (Figure 13S). This information is available free of charge via the Internet at http://pubs.acs.org/.

AUTHOR INFORMATION

Corresponding Author

*E-mail: jocrubim@unb.br or jocrubim@gmail.com − corresponding author.

Notes

The authors declare no competing financial interest.

ACKNOWLEDGMENTS

The authors thank CNPq and FAPDF for research grants. A.M.M.S.M. and A.L.P. thank CAPES for fellowships. B.A.D.N., A.F.B., M.H.S., L.M.R., and J.C.R. thank CNPq for research fellowships. The authors also thanks Dr. Alexandre Ferreira dos Santos (Universidade Tiradentes) for the viscosity measurements.

REFERENCES

(1) Veiseh, O.; Gunn, J. W.; Zhang, M. Q. *Adv. Drug Delivery Rev.* **2010**, *62*, 284−304.

(2) Jun, Y.-w.; Choi, J.-s.; Cheon, J. *Chem. Commun.* **2007**, 1203−1214.

(3) Jordan, A.; Scholz, R.; Maier-Hauff, K.; van Landeghem, F.; Waldoefner, N.; Teichgraeber, U.; Pinkernelle, J.; Bruhn, H.; Neumann, F.; Thiesen, B.; von Deimling, A.; Felix, R. *J. Neuro−Oncol.* **2006**, *78*, 7−14.

(4) Lu, A.-H.; Salabas, E. L.; Schüth, F. *Angew. Chem., Int. Ed.* **2007**, *46*, 1222−1244.
(5) Kanno, T.; Kouda, Y.; Takeishi, Y.; Minagawa, T.; Yamamoto, Y. *Tribol. Int.* **1997**, *30*, 701−705.
(6) Dupont, J.; de Souza, R. F.; Suarez, P. A. Z. *Chem. Rev.* **2002**, *102*, 3667−3691.
(7) Kabo, G. J.; Blokhin, A. V.; Paulechka, Y. U.; Kabo, A. G.; Shymanovich, M. P.; Magee, J. W. *J. Chem. Eng. Data* **2004**, *49*, 453−461.
(8) Kuwabata, S.; Tsuda, T.; Torimoto, T. *J. Phys. Chem. Lett.* **2010**, *1*, 3177−3188.
(9) Hayashi, S.; Hamaguchi, H.-o. *Chem. Lett.* **2004**, *33*, 1590−1591.
(10) Guerrero-Sanchez, C.; Lara-Ceniceros, T.; Jimenez-Regalado, E.; Raşa, M.; Schubert, U. *Adv. Mater.* **2007**, *19*, 1740−1747.
(11) Oliveira, F. C. C.; Rossi, L. M.; Jardim, R. F.; Rubim, J. C. *J. Phys. Chem. C* **2009**, *113*, 8566−8572.
(12) Jain, N.; Zhang, X. L.; Hawkett, B. S.; Warr, G. G. *ACS Appl. Mater. Interfaces* **2011**, *3*, 662−667.
(13) Rodriguez-Arco, L.; Lopez-Lopez, M. T.; Gonzalez-Caballero, F.; Duran, J. D. G. *J. Colloid Interface Sci.* **2011**, *357*, 252−254.
(14) Rodriguez-Arco, L.; Lopez-Lopez, M. T.; Duran, J. D. G.; Zubarev, A.; Chirikov, D. *J. Phys.: Condens. Matter* **2011**, *23*, 455101.
(15) Cassol, C. C.; Ebeling, G.; Ferrera, B.; Dupont, J. *Adv. Synth. Catal.* **2006**, *348*, 243−248.
(16) Abu-Reziq, R.; Wang, D.; Post, M.; Alper, H. *Adv. Synth. Catal.* **2007**, *349*, 2145−2150.
(17) Jacintho, G. V. M; Brolo, A. G.; Corio, P.; Suarez, P. A. Z.; Rubim, J. C. *J. Phys. Chem. C* **2009**, *113*, 7684−7691.
(18) Morais, P. C.; Garg, V. K; Oliveira, A. C.; Silva, L. P.; Azevedo, R. B.; Silva, A. M. L.; Lima, E. C. D. *J. Magn. Magn. Mater.* **2001**, *225*, 37−40.
(19) Gomes, J. D.; Sousa, M. H.; Tourinho, F. A.; Aquino, R.; da Silva, G. J.; Depeyrot, J.; Dubois, E.; Perzynski, R. *J. Phys. Chem. C* **2008**, *112*, 6220−6227.
(20) Sousa, M. H.; Tourinho, F. A.; Rubim, J. C. *J. Raman Spectrosc.* **2000**, *31*, 185−191.
(21) Jacintho, G. V. M; Corio, P.; Rubim, J. C. *J. Electroanal. Chem.* **2007**, *603*, 27−34.
(22) Zhang, Y.; Yang, Z.; Yin, D.; Liu, Y.; Fei, C.-L.; Xiong, R.; Shi, J.; Yan, G.-L.*J. Magn. Magn. Mater.* **2010**, *322*, 3470−3475.
(23) de Faria, D. L. A.; Silva, S. V.; Oliveira, M. T. *J. Raman Spectrosc.* **1997**, *28*, 873−878.
(24) Shebanova, O. N.; Lazor, P. *J. Solid State Chem.* **2003**, *174*, 424−430.
(25) Tang, J.; Myers, M.; Bosnick, K. A.; Brus, L. E. *J. Phys. Chem. B* **2003**, *107*, 7501−7506.
(26) Inaba, N. M., H.; Takahashi, H.; Taketomi, S.; Chikazumi, S. *IEEE Trans. Magn.* **1989**, *25*, 3866−3868.
(27) Stichauer, L.; Gavoille, G.; Simsa, Z. *J. Appl. Phys.* **1996**, *79*, 3645−3650.
(28) Woo, K.; Hong, J.; Choi, S.; Lee, H.-W.; Ahn, J.-P.; Kim, C. S.; Lee, S. W. *Chem. Mater.* **2004**, *16*, 2814−2818.
(29) Rivera-Rubero, S.; Baldelli, S. *J. Phys. Chem. B* **2006**, *110*, 4756−4765.
(30) Santos, V. O.; Alves, M. B.; Carvalho, M. S.; Suarez, P. A. Z.; Rubim, J. C. *J. Phys. Chem. B* **2006**, *110*, 20379−20385.
(31) Adachi, K.; Hirano, T. *J. Sol−Gel Sci. Technol.* **2009**, *49*, 186−195.
(32) Saha, S.; Hayashi, S.; Kobayashi, A.; Hamaguchi, H. *Chem. Lett.* **2003**, *32*, 740−741.
(33) Blokhin, A. V.; Paulechka, Y. U.; Strechan, A. A.; Kabo, G. J. *J. Phys. Chem. B* **2008**, *112*, 4357−4364.
(34) Khupse, N. D.; Kumar, A. *Indian J. Chem.* **2010**, *49A*, 635−648.
(35) Tokuda, H.; Hayamizu, K.; Ishii, K.; Susan, M. A. B. H.; Watanabe, M. *J. Phys. Chem. B* **2005**, *109*, 6103−6110.
(36) Zhang, S.; Sun, N.; He, X.; Lu, X.; Zhang, X. *J. Phys. Chem. Ref. Data* **2006**, *35*, 1475−1517.
(37) Scheeren, C. W.; Machado, G.; Teixeira, S. R.; Morais, J.; Domingos, J. B.; Dupont, J. *J. Phys. Chem. B* **2006**, *110*, 13011−13020.